JMEPEG (2018) 27:6306–6313
https://doi.org/10.1007/s11665-018-3735-6

©ASM International
1059-9495/$19.00

Thermoelectric Properties of TiNiSn Half Heusler Alloy Obtained by Rapid Solidification and Sintering

Francesco Aversano, Alberto Ferrario, Stefano Boldrini, Carlo Fanciulli, Marcello Baricco, and Alberto Castellero

(Submitted May 18, 2018; in revised form October 11, 2018; published online November 12, 2018)

Thermoelectric TiNiSn-based half Heusler compound reveals high Seebeck coefficient and electrical conductivity, leading to high power factor. As a consequence of the solidification path, TiNiSn single phase cannot be obtained directly from the liquid phase. Thus, a long annealing step is needed to homogenize the alloy. In this work, we present a new processing route for half Heusler compound formation, combining arc melting of pure elements, rapid solidification of the molten alloy and sintering. Rapid solidification of the molten alloy allows to obtain almost single TiNiSn phase, limiting the formation of the primary $TiNi_2Sn$ phase as a consequence of the deep undercooling of the liquid. The rapidly solidified alloy was ground to powder and sintered by open die pressing. As-sintered samples show a density around 95% of the theoretical value. Thermal cycling of the sintered samples shows evolution of the phases, suggesting that after sintering the sample is not in equilibrium yet. After the second thermal cycle thermoelectric properties become reproducible, indicating the attainment of the equilibrium. In conclusion, the proposed processing route allows to obtain dense TiNiSn in bulk form avoiding the time-consuming annealing step, typically used to homogenize this alloy after solidification.

Keywords intermetallics, powder metallurgy, rapid solidification, semiconductors, thermoelectricity

1. Introduction

The thermoelectric (TE) materials have recently attracted a great attention due to their solid-state use in energy harvesting from exhaust heat sources, resulting in improved energy efficiency (Ref 1, 2). The thermoelectric performance of materials is characterized by the dimensionless figure of merit $ZT = \frac{\alpha^2\sigma}{\kappa}T$, where α is the Seebeck coefficient, σ is the electrical conductivity, T is the absolute temperature, and κ is the total thermal conductivity, comprising the electronic κ_{el} and lattice κ_{lat} contributions ($\kappa = \kappa_{el} + \kappa_{lat}$)). The ideal TE material should have a high power factor $PF = \alpha^2\sigma$ and a low thermal conductivity in a wide range of temperatures. Highly efficient thermoelectric materials for power generation applications include tellurides (Ref 3, 4), skutterudites (Ref 5), Si-Ge (Ref 6, 7) and half Heusler alloys (Ref 8, 9).

Half Heusler are ternary intermetallic compounds with general formula ABX. In most cases, A and B are transition metals, while X is a main group element (Ref 10); however, the formation of half Heusler phases containing rare-earth elements can also occur (e.g., RE-Pd-Bi, where RE is a rare-earth element) (Ref 11, 12). The structure consists of three filled interpenetrating f.c.c. sublattices and one vacant f.c.c. sublattice (Wyckoff position 4d). The half Heusler compounds with valence electron count 18 have been extensively studied as potential TE materials for power generation up to 1100 K (Ref 8-16). The most studied *n*-type materials are MNiSn-based (M = Ti, Zr, Hf) compounds (Ref 17-29). The MNiSn (M = Ti, Zr, Hf) compounds are narrow-band-gap semiconductors, with an indirect band gap of the order of $\approx$ 0.1-0.2 eV (Ref 17) showing high power factor. However, relatively high values of the thermal conductivity (4 W m^{-1} K^{-1}) limit the value of ZT (0.6) and overall thermoelectric efficiency. It is well known that microstructural features, such as microstructural defects, degree of ordering (e.g., "site exchange" disorder) and second phase dispersion, can drastically influence transport properties of half Heusler compounds (Ref 18-28). For example, the effect of boundary scattering on the electron and phonon conductivities in TiNiSn-based half Heusler alloys is studied in Ref 26. It was found that grain size between 1 and 10 μm is the optimal range for reducing lattice thermal conductivity without affecting electrical conductivity (Ref 26).

Microstructural features are intimately related to the specific sample preparation techniques used. Traditionally, the TiNiSn half Heusler compounds are prepared by arc melting (Ref 27), solid-state reactions (Ref 24) and mechanical alloying (Ref 28). After arc melting, the alloy is inhomogeneous, because TiNiSn does not show congruent melting and primary solidification of $TiNi_2Sn$ full Heusler occurs upon cooling (Ref 29). Long annealing treatment (up to 3 weeks), on the one hand, improves homogeneity of the sample (Ref 27) and, on the other hand, leads to a less defective microstructure (Ref 18). Samples prepared by solid-state reactions also need long annealing time, due to the slow diffusion rates (Ref 24). Finally, mechanically alloyed samples show a more defective microstructure but are also more prone to contamination (Ref 28).

This article is an invited paper selected from presentations at "GiTE 2018" (Thermoelectricity Days), held February 21-22, 2018, in Santa Margherita Ligure, Italy, and has been expanded from the original presentation.

Francesco Aversano, Marcello Baricco, and **Alberto Castellero**, Department of Chemistry and NIS, University of Turin, Turin, Italy; **Alberto Ferrario** and **Stefano Boldrini**, Padova Unit, CNR – ICMATE, Padua, Italy; **Carlo Fanciulli**, Lecco Unit, CNR – ICMATE, Lecco, Italy. Contact e-mail: alberto.castellero@unito.it.

Rapid solidification is a non-equilibrium processing technique that typically leads to grain refining (Ref 30), supersaturation of solid solutions (Ref 31) and increase of lattice defects density (Ref 32). In the field of thermoelectric materials, rapid solidification has been successfully applied to skutterudites (Ref 33) and $AgSbTe_2$ (Ref 34), allowing rapid formation of the phase and supersaturation of the compound, respectively. In the case of (Hf,Zr)NiSn half Heusler alloys, it was shown that rapid solidification can lead to improvement of the thermoelectric properties due to the grain sizes reduction (Ref 35).

The aim of this work is to study the effect of rapid solidification on the formation of TiNiSn half Heusler phase. In order to obtain massive samples, rapidly solidified flakes were ground by hand and sintered by open die pressing (Ref 36), avoiding the annealing step. The effect of processing on the thermoelectric properties of TiNiSn is discussed in terms of structural and microstructural features of the samples.

2. Experimental Procedure

A stoichiometric TiNiSn alloy was prepared by arc melting (Edmund Bühler GmbH), starting from elemental metals (Titanium 99.99%; Nickel 99.95%; Tin 99.995%) in Argon (5.5) atmosphere. Residual traces of oxygen were removed by melting Ti and Zr getters. The button was flipped 5 times for a better homogenization. Then, arc-melted ingots were rapidly solidified by planar flow casting (Edmund Bühler GmbH), producing fragmented ribbons. The alloy was induction melted in a BN crucible under Ar (5.5) atmosphere (1 bar) and injected on a rotating copper wheel (30 ms^{-1}) by an overpressure of 0.2 bar of Ar with a distance from the wheel of 0.3 mm. The rapidly solidified ribbons were ground by hand in an agate mortar, and the powders were sintered by open die pressing (ODP) (Ref 36). The powders, loaded in a Fe sheath, were preheated at 720 °C and sintered at 475 °C for 15 min applying a compressive load of 20 tons. The shape of the sintered ODP sample is a rectangular parallelepiped with size $30 \times 30 \times 3$ mm^3. In the following of the work, arc-melted ingots, rapidly solidified ribbons, as-sintered and thermally cycled ODP samples will be named AM, RS, ODP-AP and ODP-TC, respectively, according to the legend of Table 1.

Structural characterization was carried out by x-ray diffraction (XRD) using a Bragg–Brentano geometry (XRD Panalytical XPert Pro) and Cu Kα radiation (Kα = 1.5406 Å). Rietveld analysis was performed using Maud software (Ref 37). XRD measurements were performed on ground powders in order to remove possible effects of preferential crystallographic orientations. Microstructural observations were performed by scanning electron microscopy (SEM) using a Zeiss EVO 50 XVP—LaB_6 equipped with an Oxford Instruments INCA Energy 250 for energy-dispersive x-ray analysis (EDX). Thermal stability of the samples was evaluated by differential scanning calorimetry, DSC, (Perkin Elmer DSC7). Seebeck coefficient, α, and electrical conductivity, σ, were measured under He flow in the temperature range from room temperature to 735 °C by using a custom test apparatus described in Ref 38. The relative error of α and σ values was estimated to around 4 and 5%, respectively. The thermal conductivity (κ) was calculated according to the formula $\kappa = D\rho C_p$, where D is the thermal diffusivity, C_p is the heat capacity, and ρ is the mass density. The thermal diffusivity (D) was measured between 50 and 750 °C by laser flash method (LFA 457 MicroFlash, Netzsch, Selb, Germany) with uncertainty around 3%. The mass density (ρ) was measured by Archimedean principle using a pycnometer with a relative error of $\sim$ 5%. The heat capacity (C_p) was determined using differential scanning calorimetry. In the DSC measurements of the specific heat, heating ramps at 10 K min^{-1} were performed in limited temperature ranges of 30 K. Each ramp was preceded and followed by a long isotherm in order to stabilize the signal. The measurement was repeated with the empty alumina pans, a standard (sapphire) and the annealed sintered sample. The specific heat of the sample, C_p^s, at different temperatures was obtained by comparing the signals measured for the sample and the standard using both the "height method" and the "area method" (Ref 39).

3. Results and Discussion

Figure 1(a) shows the backscattered electron image of the AM ingot. According to EDX analysis, the phases were identified as half Heusler TiNiSn (1), full Heusler $TiNi_2Sn$ (2), Ti_6Sn_5 (3), Ni_3Sn_4 (4), Ti_5Sn_3 (5), Ti (6) and Sn (7). The coexistence of more than three phases in a ternary system indicates that the AM ingot did not reach thermodynamic equilibrium, as a consequence of the relatively high cooling rate that limits chemical diffusion in the solid (Ref 40). The XRD pattern of the AM ingot is shown in Fig. 2(a), while the relative amounts of the phases and the corresponding lattice parameters, obtained by Rietveld refinement of the pattern, are reported in Table 1. Only the amount of TiNiSn, $TiNi_2Sn$, Ti_6Sn_5 and Sn phases could be quantified, because the other phases were below the detection limit.

The XRD pattern of the RS sample, Fig. 2(b), shows the presence of distinct diffraction peaks of TiNiSn phase, together with peaks with lower intensity related to $TiNi_2Sn$, Ti_6Sn_5 and Sn. The relative amount of the phases and the corresponding lattice parameters, obtained by Rietveld refinement, are reported in Table 1. The higher amount of half Heusler compound (i.e., TiNiSn) in the RS sample with respect to the AM ingot can be explained by the high degree of undercooling of the liquid during rapid solidification that inhibits the formation of the primary phase $TiNi_2Sn$. As a consequence, the metastable liquid directly solidifies as TiNiSn.

Both the XRD patterns of the AM and the RS solidified samples show around 79° a broad crystallographic reflection of the half Heusler phase (rescaled in the plot). Broadening of the peak can be caused by the presence of reduced coherent scattering domains and microstrain, suggesting the presence of a highly defective microstructure in the phase.

According to Ref 29, both TiNiSn and $TiNi_2Sn$ show an extended solubility limit for Ni as the temperature increases. At 1100 °C, the lattice parameters of the full Heusler $TiNi_{2-x}Sn$ ($0 < x < 0.34$) and the half Heusler $TiNi_{1+y}Sn$ ($0 < y < 0.22$) compounds increase as the Ni content becomes larger. In both AM and rapidly solidified RS samples, the values of refined lattice parameters of TiNiSn and $TiNi_2Sn$ significantly deviate from the reference values [a = 5.921 Å for TiNiSn (Ref 41) and a = 6.098 Å for $TiNi_2Sn$ (Ref 42)], indicating that uncontrolled solidification (i.e., arc melting and rapid solidification) leads to the formation of non-stoichiometric compounds. On the one hand, the increased value of the lattice parameter of TiNiSn (a = 5.949 Å and a = 5.946 Å for

Table 1 Results of the Rietveld refinement of the XRD patterns in Fig. 2: fitted phases, relative quantity of the phases, lattice parameter (a) of the phases

Sample	Phases	Relative quantity, wt.%	Lattice parameter, *a*, Å
AM	TiNiSn	62	5.949(1)
	$TiNi_2Sn$	26	6.075(2)
	Ti_6Sn_5	9	…
	Sn	3	…
RS	TiNiSn	84	5.946(8)
	$TiNi_2Sn$	10	6.058
	Ti_6Sn_5	3	…
	Sn	3	…
ODP-AP	TiNiSn_1	58	5.928(3)
	TiNiSn_2	38	5.945(4)
	$TiNi_2Sn$	1	6.071(8)
	Ni_3Sn_4	3	…
ODP-TC	TiNiSn	91	5.922(2)
	$TiNi_2Sn$	6	6.082(9)
	Ni_3Sn_4	3	…

Arc-melted (AM), rapidly solidified (RS), as-prepared open die pressed (ODP-AP), open die pressed after thermal cycling (ODP-TC)

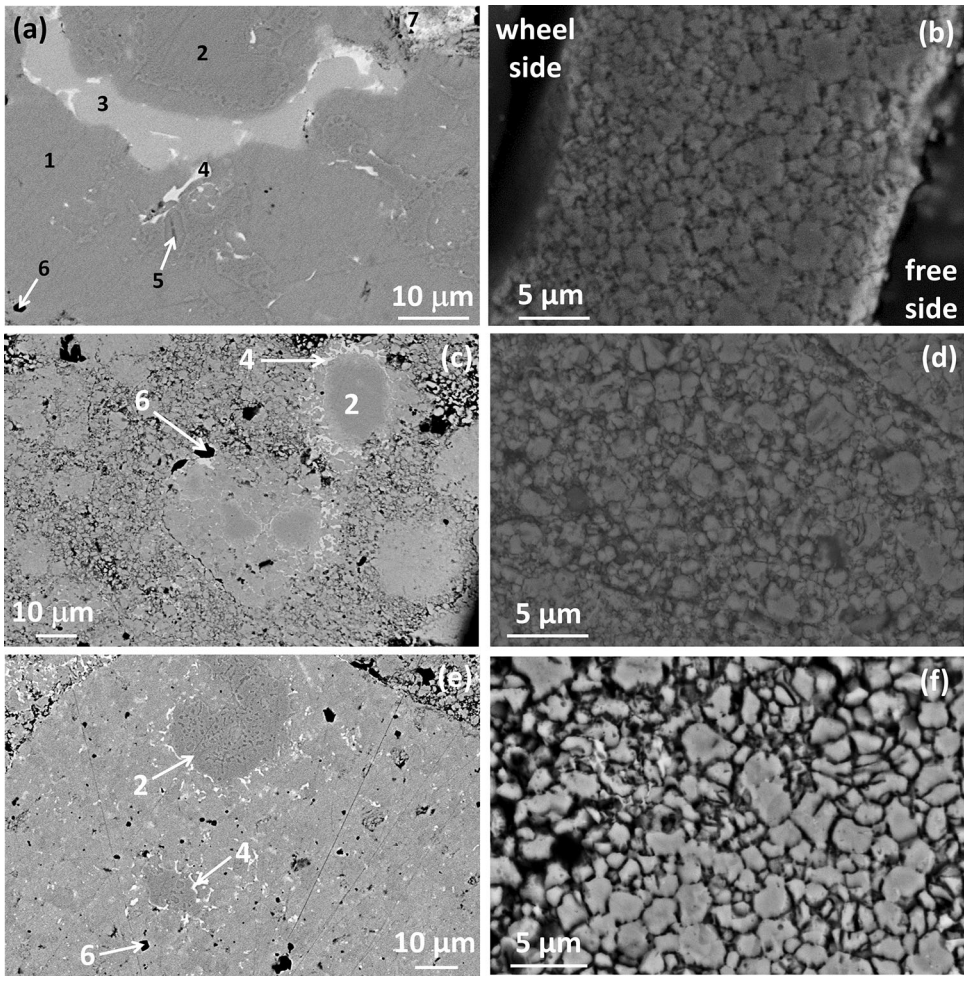

Fig. 1 (a) Backscattered electron SEM micrograph of the arc-melted (AM) TiNiSn master alloy. (b) Secondary electron SEM micrograph of the rapidly solidified (RS) ribbon after chemical etching. (c) Backscattered electron SEM micrograph of the as-sintered sample (ODP-AP). (d) Secondary electron SEM micrograph of the as-sintered sample (ODP-AP) after chemical etching. (e) Backscattered electron SEM micrograph of the sintered sample after cycle 2 in the TE measurements (ODP-TC). (f) Secondary electron SEM micrograph of the etched sintered sample after cycle 2 in the TE measurements (ODP-TC). Legend of the phases for micrographs (a), (c) and (e): TiNiSn (1), $TiNi_2Sn$ (2), Ti_6Sn_5 (3), Ni_3Sn_4 (4), Ti_5Sn_3 (5), Ti (6), Sn (7)

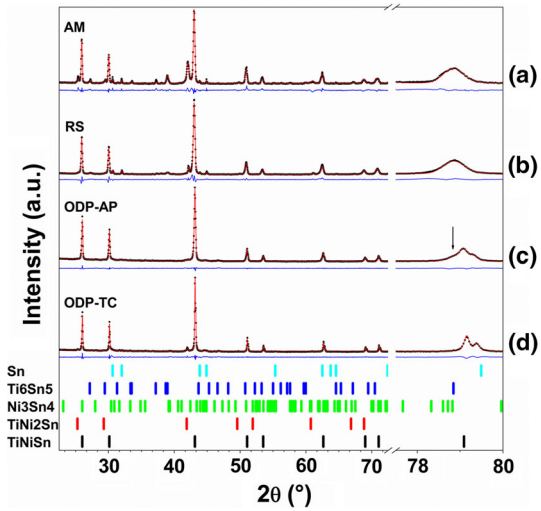

Fig. 2 XRD patterns of arc-melted (AM) ingot (a) rapidly solidified (RS) sample (b), as-sintered (ODP-AP) sample (c) and sintered sample after cycle 2 in the TE measurements (ODP-TC) (d). Black dots and red lines represent experimental data and fitted patterns, respectively; the blue lines are the difference between experimental data and the corresponding fitted patterns. Bars indicate the diffraction peaks positions for the various phases (Color figure online)

AM and RS samples, respectively) with respect to the reference value [a = 5.921 Å (Ref 41)] can be explained by supersaturation of the cell with Ni. On the other hand, the decreased value of the lattice parameter of $TiNi_2Sn$ (a = 6.075 Å and a = 6.058 Å for AM and RS samples, respectively) with respect to the reference value [a = 6.098 Å (Ref 42)] reveals a lower amount of Ni in the cell. The amount of Ni present in the half and full Heusler phases in the AM and RS samples is very close to the solubility limit around 950 °C, indicating that no compositional variation occurred in the two phases during cooling below this temperature.

Rapid solidification also leads to refinement of the microstructure that reveals a grain size between 1 µm and 5 µm, as shown in Fig. 1(b). The microstructure is finer on the wheel side with respect to the free side, due to the higher cooling rate when the liquid directly solidifies in contact with the copper wheel. Thermal cycling in the DSC of the RS sample (not reported) shows the disappearance of the endothermic peak around 232 °C, related to the melting of the residual amount of elemental Sn, indicating homogenization of the sample.

The backscattered electron image of the ODP-AP sample is reported Fig. 1(c), and it shows the presence of the half Heusler TiNiSn compound in the matrix and full Heusler $TiNi_2Sn$, Ti and Ni_3Sn_4 as secondary phases. The presence of Ti is not expected on the basis of the thermodynamic equilibrium (Ref 29). Since the alloy was kept in the molten state only for a tenth of seconds before rapid solidification, it is likely that the unreacted Ti originally present in the AM ingot, Fig. 1(a), did not have time to fully dissolve into the liquid phase. The secondary electron image of the ODP-AP after chemical etching, Fig. 1(d), shows a fine microstructure that is comparable to the one of the RS sample. On the basis of the melting point value of the alloy [$T_m \cong 1250$ °C (Ref 29)], the recrystallization temperature (i.e., 0.5 T_m) was estimated around 490 °C. Thus, grain growth was limited during sintering because the pre-annealing was conducted at 720 °C for only 5 min and the pressing at 475 °C for 15 min.

Figure 2(c) shows the XRD pattern of the ODP-AP sample, while Table 1 reports the relative amount of the phases and the corresponding lattice parameters, obtained by Rietveld refinement. The amount of unreacted Ti, shown in Fig. 1(c), is below the detection limit and was not quantified. The crystallographic reflection around 79°, corresponding to the half Heusler TiNiSn, is narrower than in the RS ribbon (the peaks due to $K\alpha_1$ and $K\alpha_2$ are partially resolved), and it shows a shoulder on the left (indicated by the arrow) that can be fitted by a second TiNiSn phase (TiNiSn_2). TiNiSn_2 shows a larger lattice parameter (a = 5.945 Å) than the one of TiNiSn_1 (a = 5.928 Å), corresponding to the main peak. The values of the lattice parameters of TiNiSn_1 and TiNiSn_2 are, respectively, smaller and comparable to the one of the half Heusler phase in the RS ribbon (a = 5.946 Å). The value of the lattice parameter of the full Heusler phase $TiNi_2Sn$ (a = 6.071 Å) is increased with respect to the one in the RS ribbons (a = 6.058 Å). The change of the lattice parameters in the half and full Heusler phases in the ODP-AP sample with respect to the RS ribbons is related to the decreased Ni content in TiNiSn_1 and the larger filling of the $TiNi_2Sn$ cell with Ni and is due to the narrowed solubility range as the temperature decreases.

Figure 3 shows the DSC trace for the ODP sintered sample (10 K min^{-1}) upon heating and cooling, repeated for two consecutive cycles. The DSC trace of the ODP-AP sample (first cycle) shows upon heating a broad endothermic signal, starting around 315 °C, that is absent in the case of the ODP-TC sample (second cycle). Both the calorimetric traces of ODP-AP and ODP-TC samples show upon heating an endothermic peak just above 690 °C, that is reversed upon cooling. According to Ref 29, this signal can be related to the reversible reaction

$$3TiNiSn + Ni_3Sn_4 \rightarrow 3TiNi_2Sn + 4Sn(liq) \qquad \text{(Eq 1)}$$

Thermoelectric properties of the ODP sintered material were measured as a function of temperature over two cycles, as shown in Fig. 4. The first and second cycles are related to ODP-AP and ODP-TC samples, respectively. The effect of thermal cycling during TE measurements on structural and microstructural features was investigated.

The backscattered electron image of the ODP-TC sample, Fig. 1(e), shows the same phases and similar microstructure of the ODP-AP sample. Observations of the etched sample with the secondary electron detector, Fig. 1(f), do not reveal significant grain growth with respect to the ODP-AP sample.

Figure 2(d) shows the XRD pattern of the ODP-TC sample, while the results of the quantitative analysis, obtained by Rietveld refinement, are reported in Table 1. In the ODP-TC sample, the relative amount of full Heusler phase increases, whereas that of half Heusler phase decreases, and the values of the lattice parameters of the two phases become close the to the equilibrium ones. Upon heating, the supersaturated half Heusler phase (TiNiSn_2), originally present in the ODP-AP sample, progressively rejected Ni in excess, leading to the precipitation of stoichiometric $TiNi_2Sn$.

According to the previous structural and microstructural analysis, the irreversible endothermic signal observed in the DSC trace starting from 315 °C, Fig. 3, can be related to a progressive evolution of the ODP-AP sample toward the equilibrium.

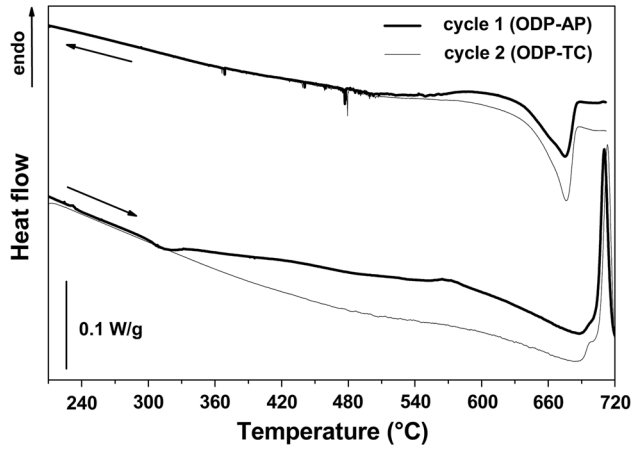

Fig. 3 DSC traces (10 K min^{-1}) of the sintered sample. Thick and thin lines indicate the first and the second cycles, corresponding to ODP-AP and ODP-TC samples, respectively

Seebeck coefficient, Fig. 4(a), is negative revealing, as expected, an *n*-type behavior. For sake of clarity, we will refer to the absolute value of the Seebeck coefficient $|\alpha|$. In the ODP-AP sample (cycle 1), $|\alpha|$ shows an increasing trend from room temperature to 310 °C, a sudden change in slope (marked by the arrow) around 310 °C, an almost linear decrease with temperature up to about 700 °C and, finally, an abrupt decrease between 700 and 710 °C (marked by the arrow). ODP-TC (second cycle) shows a lower value of $|\alpha|$ with respect to ODP-AP (first cycle). The change in slope becomes smoother and is shifted to high temperature (460-470 °C). Again, there is an abrupt variation of $|\alpha|$ between 700 and 710 °C.

The electrical conductivity, Fig. 4(b), shows an increasing trend with temperature indicating a typical semiconducting behavior. In the first cycle (ODP-AP), there is an increase in the slope around 310 °C followed by a sudden increase of σ around 700-710 °C. The latter appears also in the second cycle (ODP-TC). In the second cycle, the electrical conductivity shows larger values than in the first cycle. The difference between the two cycles becomes less marked at high temperature.

The slope change around 310 °C, observed during the first cycle of the measurement of Seebeck coefficient and electrical conductivity, can be related to the irreversible endothermic broad peak starting at 315 °C in the first DSC cycle, Fig. 3. Furthermore, the sudden variation of $|\alpha|$ and σ around 700-710 °C, observed both during the first and second cycles of the measurement of Seebeck coefficient and electrical conductivity, can be related to the reversible reaction (1) observed in the DSC trace.

ODP-TC sample shows an increase of thermal diffusivity (D) between room temperature and 600 °C (cycle 2) with respect to the ODP-AP sample (cycle 1), as shown in Fig. 4(c). The thermal conductivity (κ_{tot}) has been calculated using the equation $\kappa = D\rho C_p$, where D is the thermal diffusivity reported in Fig. 4(c), ρ is the mass density, measured as 6.82 g cm^{-3} (both for ODP-AP and ODP-TC samples), and C_p is the specific heat determined by DSC. For C_p, an average value of 0.331 ± 0.007 J g^{-1} K^{-1} (or 24.86 ± 0.52 J mol^{-1} K^{-1}) was considered over the whole temperature range, since measured values scatter between 0.321 and 0.338 J g^{-1} K^{-1} without a clear temperature dependence. The relative error obtained for C_p ($\sim 2\%$) is in agreement with the typical values for this technique. The value of C_p obtained is very close to $3R$ (where R is the gas constant), validating the Dulong–Petit approximation that is typically used for this alloy in the considered temperature range. The obtained values for κ_{tot} are reported in Fig. 4(d). They show a trend similar to D in Fig. 4(c), as expected from the selected constant values for ρ and C_p. The electronic contribution to the thermal conductivity was estimated through the Wiedemann–Franz law, $\kappa_{el} = L\sigma T$ (where L is Lorenz's constant, 2 10^{-8} V^2 K^{-2}, σ is the electrical conductivity, and T is the absolute temperature). Because of the increase of σ after thermal cycling, also κ_{el} becomes larger in the second cycle over the whole temperature range. From the difference between κ_{tot} and κ_{el}, the value of the lattice contribution to the thermal conductivity, κ_{lat}, was estimated.

The effect of secondary phases (typically $TiNi_2Sn$) on thermoelectric properties of TiNiSn alloy was extensively investigated in the literature (Ref 19-22). As the amount of $TiNi_2Sn$ increases, the electrical conductivity increases and the absolute value of Seebeck coefficient $|\alpha|$ decreases, according to the metallic behavior of the secondary phase (Ref 19-22). The opposite effect of the metallic secondary phases on σ and $|\alpha|$ leads, on the one hand, to maximum values of power factor for 5% (Ref 20) and 13% of $TiNi_2Sn$ (Ref 21), and, on the other hand, a monotonous decrease of power factor with $TiNi_2Sn$ content (Ref 22). Concerning thermal conductivity, a decrease of lattice thermal conductivity is observed as the amount of secondary phases increases (Ref 19-21) due to the phonon scattering of inclusions.

Discrepancies between values of thermoelectric properties of single-phase TiNiSn reported in the literature can be rationalized by the different amount of Ni dissolved in the half Heusler structure (Wyckoff position 4d) (Ref 23). According to the phase diagram, TiNiSn shows stable boundary compositions that differ in Ni content by 6 at.% (Ref 23). In Ni-rich TiNiSn, the partial occupancy of the Wyckoff position 4d leads to a lower value of the band gap, together with enhanced electron and phonon scattering, and consequently to higher values of Seebeck coefficient, $|\alpha|$, and lower values of electrical and thermal conductivities with respect to Ni-poor stoichiometric TiNiSn (Ref 23). However, phonon scattering is larger than electron scattering, leading to a larger ZT value in the Ni-rich compound (Ref 23).

The variation of the thermoelectric properties between the ODP-AP sample (cycle 1) and the ODP-TC sample (cycle 2) can be explained by the evolution of the sample from the microstructural and structural point of view. In the ODP-AP sample, there is a larger amount of half Heusler phase (Table 1) with respect to the ODP-TC sample, and both half Heusler and full Heusler phases are out of equilibrium, since they are supersaturated and depleted in Ni, respectively. After thermal cycling, thermodynamic equilibrium is attained, half Heusler and full Heusler compounds become stoichiometric, and the relative quantity of $TiNi_2Sn$ increases, leading to a decrease of $|\alpha|$ and an increase of electrical conductivity (ODP-TC). Consequently, the power factor of the ODP-TC sample is lowered with respect to the ODP-AP one because of its dependence from the square of the Seebeck coefficient, Fig. 4(e). Both ODP-AP and ODP-TC samples show lower values of $|\alpha|$ and larger values of σ with respect to those reported in the literature for single-phase TiNiSn (see for instance Ref 19, 21-23). As already mentioned above, this discrepancy can be explained by the presence of secondary metallic phases (i.e., $TiNi_2Sn$ and Ni_3Sn_4).

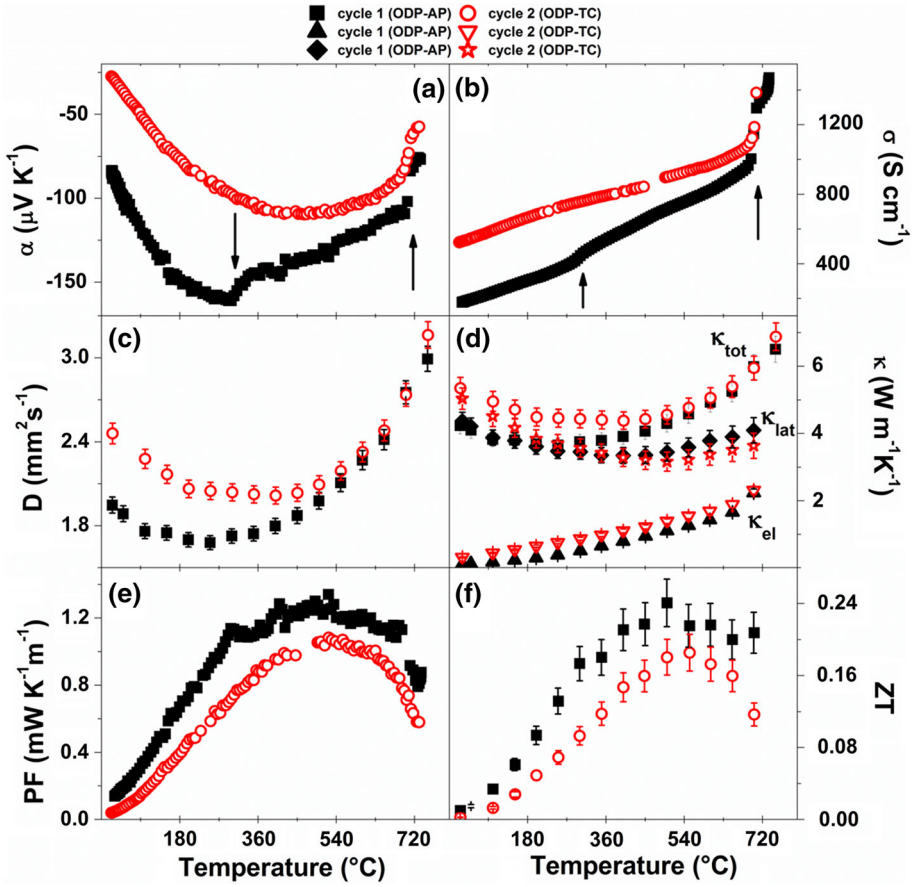

Fig. 4 Temperature dependence of Seebeck coefficient, α, (a), electrical conductivity, σ, (b), thermal diffusivity, D, (c), thermal conductivity, κ, (d), power factor, PF, (e) and figure of merit, *ZT*, (f), of the sintered sample during the first cycle, ODP-AP, (black symbols) and the second cycle, ODP-TC, (red open symbols). The relative error of the measured values is 4% for α, 5% for σ and 3% for D. The relative error of calculated properties, obtained considering the propagation of errors between independent variables, is 6% for κ, 9% for PF and 11% for *ZT*. For graphical reasons, error bars are shown only for D (panel c), κ (panel d) and *ZT* (panel f) (Color figure online)

In the case of thermal conductivity, the larger values shown after thermal cycling can be explained by the larger values of κ_{el} and κ_{lat}. In ODP-TC, κ_{lat} shows larger values than the ODP-AP sample between room temperature and 350 °C. From this temperature, the two samples show similar values of κ_{lat}. Equilibrium half Heusler and full Heusler compounds, formed upon annealing, show a less effective phonon scattering with respect to the corresponding defective phases originally present in the ODP-AP sample. The precipitation of a larger amount of secondary phases is not able to compensate the decreased phonon scattering of the matrix, leading to larger values of lattice thermal conductivity. The effect of grain boundary scattering before and after thermal cycling can be considered unchanged since no significant grain growth was induced by the thermal treatment. The measured values of thermal conductivity are comparable with those typically reported in the literature (see for example Ref 19, 21-23).

The overall thermoelectric performance is represented by the figure of merit, *ZT*, as reported in Fig. 4(f). Around 540 °C, *ZT* shows maximum values of 0.24 and 0.18 for the ODP-AP sample and ODP-TC sample, respectively. The decrease of *ZT* after thermal cycling is due either to the decrease of the power factor and the increase of the thermal conductivity.

4. Conclusions

In this work, dense TiNiSn bulk samples were obtained by combining arc melting, rapid solidification by planar flow casting and sintering by open die pressing. Upon rapid quenching, primary solidification of $TiNi_2Sn$ is hindered and almost TiNiSn single phase was obtained without the need of time-consuming annealing step. After rapid solidification, both TiNiSn and $TiNi_2Sn$ are out of equilibrium, since they are super saturated and depleted in Ni, respectively. Dense massive samples were obtained by sintering the rapidly solidified alloy. However, as-sintered samples are thermodynamically metastable. In fact, thermal cycling of the sintered sample during thermoelectric measurements leads to the transformation of defective metastable TiNiSn and $TiNi_2Sn$ into the corresponding stoichiometric equilibrium compounds.

The structural and microstructural evolution of the as-sintered sample upon thermal cycling affects thermoelectric properties. Thermally cycled sample shows a more metallic behavior with respect to the as-sintered one, with larger values of electrical conductivity and lower values of Seebeck coefficient, |α|, as consequence of the larger amount of metallic secondary phases ($TiNi_2Sn$ and Ni_3Sn_4) and the less defective microstructure. Meanwhile, transformation of defective

metastable TiNiSn and $TiNi_2Sn$ into the corresponding stoichiometric equilibrium compounds leads to lower phonon scattering, that is not compensated by the larger fraction of secondary phases dispersed in the half Heusler matrix.

Acknowledgments

Alberto Castellero thanks University of Turin and Compagnia di Sanpaolo for financial support (Project No. CSTO162398). The authors also thank Dr. G. Fiore (University of Turin) and Mr E. Bassani (CNR-ICMATE, Unità di Lecco) for the support in the arc melting and ODP processing of the samples, respectively.

References

1. F.J. DiSalvo, Thermoelectric Cooling and Power Generation, *Science*, 1999, **285**, p 703–706
2. M. Zebarjadi, K. Esfarjani, M.S. Dresselhaus, Z.F. Ren, and G. Chen, Perspectives on Thermoelectrics: From Fundamentals to Device Applications, *Energy Environ. Sci.*, 2012, **5**(1), p 5147–5162
3. B. Dado, Y. Gelbstein, D. Mogilansky, V. Ezersky, and M.P. Dariel, Structural Evolution Following Spinodal Decomposition of the Pseudo-Ternary Compound $(Pb_{0.3}Sn_{0.1}Ge_{0.6})Te$, *J. Electron. Mater.*, 2010, **39**(9), p 2165–2171
4. Y. Gelbstein, Z. Dashevsky, and M.P. Dariel, Highly Efficient Bismuth Telluride Doped p-Type $Pb_{0.13}Ge_{0.87}Te$ for Thermoelectric Applications, *Phys. Status Solidi (RRL)*, 2007, **1**(6), p 232–234
5. G. Rogl and P. Rogl, Skutterudites, a Most Promising Group of Thermoelectric Materials, *Curr. Opin. Green Sustain. Chem.*, 2017, **4**, p 50–57
6. D.M. Rowe, V.S. Shukla, and N. Savvides, Phonon Scattering at Grain Boundaries in Heavily Doped Fine-Grained Silicon-Germanium Alloys, *Nature*, 1981, **290**(5809), p 765–766
7. C.B. Vining, W. Laskow, J.O. Hanson, R.R. Van Der Beck, and P.D. Gorsuch, Thermoelectric Properties of Pressure-Sintered $Si_{0.8}Ge_{0.2}$ Thermoelectric Alloys, *J. Appl. Phys.*, 1991, **69**(8), p 4333–4340
8. O. Appel, T. Zilber, S. Kalabukhov, O. Beeri, and Y. Gelbstein, Morphological Effects on the Thermoelectric Properties of $Ti_{0.3}Zr_{0.35}Hf_{0.35}Ni_{1+\delta}Sn$ Alloys Following Phase Separation, *J. Mater. Chem. C*, 2015, **3**(44), p 11653–11659
9. O. Appel, M. Schwall, M. Kohne, B. Balke, and Y. Gelbstein, Microstructural Evolution Effects of Spark Plasma Sintered $Ti_{0.3}Zr_{0.35}Hf_{0.35}NiSn$ Half-Heusler Compound on the Thermoelectric Properties, *J. Electron. Mater.*, 2013, **42**(7), p 1340–1345
10. J. Krez and B. Balke, Thermoeletric Heusler Compounds, *Heusler Alloys: Properties, Growth, Applications*, C. Felser and A. Hirohata, Ed., Springer, Cham, 2016, p 249–267
11. K. Gofryk, D. Kaczorowski, T. Plackowski, A. Leithe-Jasper, and Y. Grin, Magnetic and Transport Properties of Rare-Earth-Based Half-Heusler Phases RPdBi: Prospective Systems for Topological Quantum Phenomena, *Phys. Rev. B*, 2011, **84**(3), p 035208
12. O. Pavlosiuk, X. Fabreges, A. Gukasov, M. Meven, D. Kaczorowski, and P. Wiśniewski, Magnetic Structures of REPdBi Half-Heusler Bismuthides (RE = Gd, Tb, Dy, Ho, Er), *Physica B*, 2018, **536**, p 56–59
13. J.-W.G. Bos and R.A. Downie, Half-Heusler Thermoelectric: A Complex Class of Materials, *J. Phys. Condens. Matter*, 2014, **26**(43), p 433201
14. R. Gautier, X. Zhang, L. Hu, L. Yu, Y. Lin, T.O.L. Sunde, D. Chon, K.R. Poeppelmeier, and A. Zunger, Prediction and Accelerated Laboratory Discovery of Previously Unknown 18-Electron ABX Compounds, *Nat. Chem.*, 2015, **7**(4), p 308–316
15. T. Zhu, C. Fu, H. Xie, Y. Liu, and X. Zhao, High Efficiency Half-Heusler Thermoelectric Materials for Energy Harvesting, *Adv. Energy Mater.*, 2015, **5**(19), p 1500588
16. L. Huang, Q. Zhang, B. Yuan, X. Lai, X. Yan, and Z. Ren, Recent Progress in Half-Heusler Thermoelectric Materials, *Mater. Res. Bull.*, 2016, **76**, p 107–112
17. F.G. Aliev, A.I. Belogorokhov, N.B. Brandt, V.V. Kozyr'kov, R.V. Skolozdra, and Y.V. Stadnyk, Optical Properties of the Vacancy MNiSn Lattices (M = Ti, Zr, Hf), *JETP Lett.*, 1988, **47**(3), p 184–187
18. C. Uher, J. Yang, S. Hu, D.T. Morelli, and G.P. Meisner, Transport Properties of Pure and Doped MNiSn (M = Zr, Hf), *Phys. Rev. B*, 1999, **59**(13), p 8615–8621
19. C.S. Birkel, J.E. Douglas, B.R. Lettiere, G. Seward, N. Verma, Y. Zhang, T.M. Pollock, R. Seshadri, and G.D. Stucky, Influence of Ni Nanoparticle Addition and Spark Plasma Sintering on the TiNiSn-Ni System: Structure, Microstructure and Thermoelectric Properties, *Solid State Sci.*, 2013, **26**, p 16–22
20. C.S. Birkel, J.E. Douglas, B.R. Lettiere, G. Seward, N. Verma, Y. Zhang, T.M. Pollock, R. Seshadri, and G.D. Stucky, Improving the Thermoelectric Properties of Half-Heusler TiNiSn Through Inclusion of a Second Full-Heusler Phase: Microwave Preparation and Spark Plasma Sintering of $TiNi_{1+x}Sn$, *Phys. Chem. Chem. Phys.*, 2013, **15**(18), p 6990–6997
21. J.E. Douglas, C.S. Birkel, N. Verma, V.M. Miller, M.-S. Miao, G.D. Stucky, T.M. Pollock, and R. Seshadri, Phase Stability and Property Evolution of Biphasic Ti-Ni-Sn Alloys for Use in Thermoelectric Applications, *J. Appl. Phys.*, 2014, **115**(4), p 043720
22. R.A. Downie, R.I. Smith, D.A. MacLaren, and J.-W.G. Bos, Metal Distributions, Efficient n-Type Doping, and Evidence for in-Gap States in $TiNiM_ySn$ (M = Co, Ni, Cu) half-Heusler nanocomposites, *Chem. Mater.*, 2015, **27**(7), p 2449–2459
23. Y. Tang, X. Li, L.H.J. Martin, E. Cuervo Reyes, T. Ivas, C. Leinenbach, S. Anand, M. Peters, G.J. Snyder, and C. Battaglia, Impact of Ni Content on the Thermoelectric Properties of Half-Heusler TiNiSn, *Energy Environ. Sci.*, 2018, **11**(2), p 311–320
24. S.A. Barczak, J. Buckman, R.I. Smith, A.R. Baker, E. Don, I. Forbes, and J.-W.G. Bos, Impact of Interstitial Ni on the Thermoelectric Properties of the Half-Heusler TiNiSn, *Materials*, 2018, **11**(4), p 536
25. M. Schrade, K. Berland, S.N.H. Eliassen, M.N. Guzik, C. Echevarria-Bonet, M.H. Sørby, P. Jenuš, B.C. Hauback, R. Tofan, A.E. Gunnæs, C. Persson, O.M. Løvvik, and T.G. Finstad, The Role of Grain Boundary Scattering in Reducing the Thermal Conductivity of Polycrystalline XNiSn (X = Hf, Zr, Ti) Half-Heusler Alloys, *Sci. Rep.*, 2017, **7**(1), p 13760
26. S. Bhattacharya, M.J. Skove, M. Russell, T.M. Tritt, Y. Xia, V. Ponnambalam, S.J. Poon, and N. Thadhani, Effect of Boundary Scattering on the Thermal Conductivity of TiNiSn-Based Half-Heusler Alloys, *Phys. Rev. B*, 2008, **77**(18), p 184203
27. B.A. Cook, J.L. Harringa, Z.S. Tan, W.A. Jesser, TiNiSn: A Gateway to the (1,1,1) Intermetallic Compounds, in *15th International Conference on Thermoelectrics, 26–29 March 1996* (IEEE, Pasadena, CA, 1996), pp. 122–127
28. M. Zou, J.-F. Li, B. Du, D. Liu, and T. Kita, Fabrication and Thermoelectric Properties of Fine-Grained TiNiSn Compounds, *J. Solid State Chem.*, 2009, **182**(11), p 3138–3142
29. M. Gürth, A. Grytsiv, J. Vrestal, V.V. Romaka, G. Giester, E. Bauer, and P. Rogl, On the Constitution and Thermodynamic Modelling of the System Ti-Ni-Sn, *RSC Adv.*, 2015, **5**(112), p 92270–92291
30. M. Baricco, E. Bosco, E. Olivetti, M. Palumbo, P. Rizzi, A. Stantero, and L. Battezzati, Rapid Solidification of Alloys, *Int. J. Mater. Prod. Technol.*, 2004, **20**(5–6), p 358–376
31. D. Lussana, A. Castellero, M. Vedani, D. Ripamonti, G. Angella, and M. Baricco, Microstructure Refinement and Hardening of Ag–20 wt% Cu Alloy by Rapid Solidification, *J. Alloys Compd.*, 2014, **615**(S1), p S633–S637
32. D. Lussana, A. Castellero, D. Ripamonti, G. Angella, M. Vedani, A. Zambon, and M. Baricco, Effect of Rapid Quenching and Severe Plastic Deformation on Silver, *Int. J. Mater. Res.*, 2012, **103**(9), p 1117–1121
33. C. Artini, A. Castellero, M. Baricco, M.T. Buscaglia, and R. Carlini, Structure, Microstructure and Microhardness of Rapidly Solidified $Sm_y(Fe_xNi_{1-x})_4Sb_{12}$ (x = 0.45, 0.50, 0.70, 1) Thermoelectric Compounds, *Solid State Sci.*, 2018, **79**, p 71–78
34. A. Castellero, G. Fiore, E. Evenstein, M. Baricco, and Y. Amouyal, Effects of Rapid Solidification on Phase Formation and Microstructure Evolution of $AgSbTe_2$-Based Thermoelectric Compounds, *J. Nanosci. Nanotechnol.*, 2017, **17**(3), p 1650–1656
35. Yu Cui, T.-J. Zhu, K. Xiao, J.-J. Shen, S.-H. Yang, and X.-B. Zhao, Reduced Grain Size and Improved Thermoelectric Properties of Melt Spun (Hf, Zr)NiSn Half-Heusler Alloys, *J. Electron. Mater.*, 2010, **39**(9), p 2008–2012

36. S. Ceresara, C. Fanciulli, F. Passaretti, and D. Vasilevskiy, Texturing of $(Bi_{0.2}Sb_{0.8})_2$ Te_3 Nanopowders by Open Die Pressing, *J. Electron. Mater.*, 2013, **42**(7), p 1529–1534
37. http://maud.radiographema.com
38. S. Boldrini, A. Famengo, F. Montagner, S. Battiston, S. Fiameni, M. Fabrizio, and S. Barison, Test rig for High-Temperature Thermopower and Electrical Conductivity Measurements, *J. Electron. Mater.*, 2013, **42**(7), p 1319–1323
39. R.F. Speyer, *Thermal Analysis of Materials*, Marcel Dekker Inc., New York, 1994, p 79–80
40. D.A. Porter and K.E. Easterling, *Phase Transformations in Metals and Alloys*, 2nd ed., Chapman & Hall, New York, 1992, p 208–214
41. International Center for Diffraction Data, Powder Diffraction File 03-065-0991
42. International Center for Diffraction Data, Powder Diffraction File 00-052-0905